JACS
JOURNAL OF THE AMERICAN CHEMICAL SOCIETY
pubs.acs.org/JACS
Article

Anti-biopassivated Reticular Micromotors for Bladder Cancer Therapy

Jun Sun,[§] Ran Chu,[§] Xiaoqian Wu, Qian Yu, Wencheng Xiao, Hang Ao, Yuru Wang, Taikang Wu, Huangxian Ju, Jie Wu,* and Jianping Lei*

Cite This: J. Am. Chem. Soc. 2025, 147, 17936−17945
Read Online

ABSTRACT: The limited lifespan of enzyme-powered micro/nanomotors (MNMs) hinders their biomedical applications due to the easy deactivation in tumor microenvironments. In this study, by taking advantage of hydrogen bond-rich metal-organic frameworks (MOFs), we design anti-biopassivated urease-powered MOF motors (Ur-MOFtors) with sustained motility for bladder cancer therapy. Such reticular Ur-MOFtors exhibited an exceptionally long locomotion lifespan exceeding 90 min in highly concentrated urea, which was an 18-fold enhancement compared with urease-adsorbed MOFs, resulting in excellent anti-biopassivation of MOFtors. The underlying molecular mechanism of persistent motion involves hydrogen bonding interaction between the MOF skeleton and the catalytic product, as identified by *in situ* infrared spectroscopy and density functional theory. Based on the preserved enzymatic activity comparable to native urease, the self-propulsion pathway of Ur-MOFtors is driven by ionic self-diffusiophoresis with the positive chemotactic motion toward urea. Benefiting from the persistent motion of Ur-MOFtors in physiological urea, a rapid bladder cancer therapy was achieved with few instillation sessions and short treatment cycles during intravesical administration. This hydrogen bond-rich framework presents a promising anti-biopassivated approach to overcoming the short lifespan and easy deactivation of enzymatic motors for advanced therapeutic robotics.

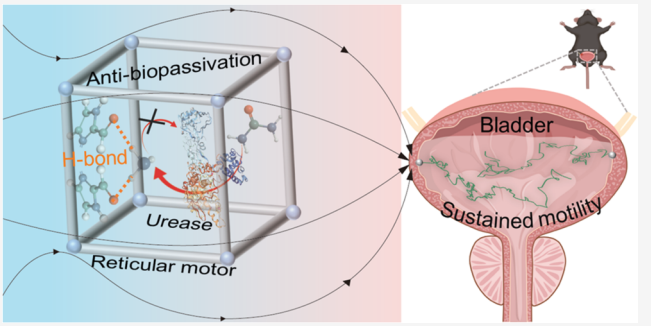

INTRODUCTION

Inspired by the active motion of specific natural systems, artificial micro/nanomotors (MNMs) that self-propel by consuming environmental energy have garnered increasing attention in the last decades.[1,2] Among these, enzyme-powered MNMs exhibit significant advantages of biocompatibility, versatility, and substrate availability in various fields, particularly for biomedical applications.[3−5] Typically, urease-powered MNMs (Ur-MNMs) have proven highly effective as tools for *in vivo* diagnostic and therapeutic applications.[6−9] For example, to realize active binding and targeted delivery to cancer cells and bacteria, Wang's group developed urease-powered Janus platelet cell robots by asymmetrically immobilizing urease onto the surface of platelet cells with intrinsic biofunctionalities.[10] Moreover, a universal urease-powered nanobot was pioneered based on hollow mesoporous silica nanoparticles for radionuclide bladder cancer therapy in Sanchez's group,[11] following with fluorescence, ultrasound, and magnetic resonance imaging in Ma's group.[12] The enhanced motility of micromotors functionalized with the purified urease further emphasizes the influence of urease activity on the motion performance of Ur-MNMs.[13] Since urease easily deactivates at high concentrations of urea and produced ammonia,[14−17] preserving urease activity and enhancing Ur-MNMs lifetime hold great challenges in the biomedical field.[18,19]

Recently, metal-organic frameworks (MOFs), a class of porous crystalline polymers with metal nodes connected by organic linkers, have been reported as protective exteriors for enzyme stabilization due to their unique reticular properties, including high surface area, tunable porosity, thermal stability, biodegradability, and biocompatibility.[20−23] The integration of flexible MOFs with native enzymes has also led to the creation of stable enzyme-powered MOF motors (E-MOFtors), offering a viable route for realizing active cellular uptake and tissue penetration.[24] Typically, medical-oriented E-MOFtors are fabricated using pre-design methods, such as the *de novo* approach to encapsulate enzymes within MOFs,[25] or post-synthetic methods,[26] such as physical adsorption or chemical cross-linking, to anchor enzymes to the pore or surface of MOFs. A urease-encapsulated zeolitic imidazolate framework-8

Received: February 17, 2025
Revised: April 29, 2025
Accepted: May 6, 2025
Published: May 16, 2025

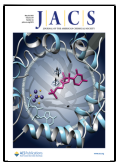

https://doi.org/10.1021/jacs.5c02949
J. Am. Chem. Soc. 2025, 147, 17936−17945

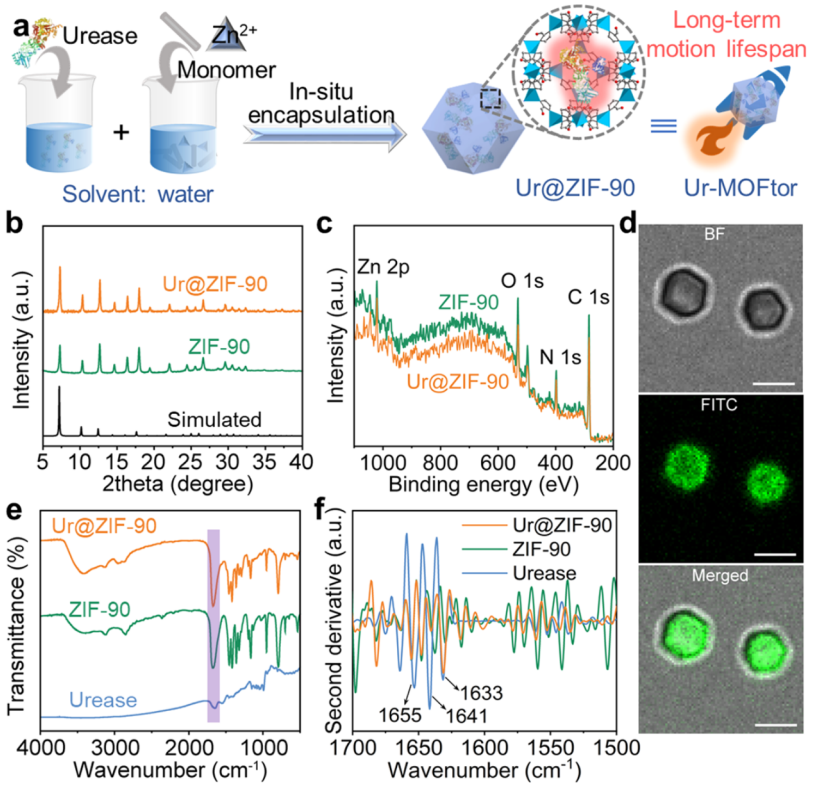

Figure 1. Synthesis and characterization of Ur-MOFtors. (a) The preparation process of anti-biopassivated Ur-MOFtors with long-term motion lifespan. (b) XRD patterns of Ur@ZIF-90, ZIF-90, and simulated ZIF-90. (c) XPS patterns of Ur@ZIF-90 and ZIF-90. (d) Confocal fluorescence images of FITC-labeled Ur@ZIF-90 (scale bar: 2 μm). (e) FTIR spectra and the corresponding (f) second derivative FTIR spectra (vector normalized in the spectral region of 1700−1500 cm^{-1}) of Ur@ZIF-90, ZIF-90, and urease.

(ZIF-8) nanomotor was established to protect urease from harsh conditions for enhanced penetration capability in the pig small intestine.[27] To optimize the performance of E-MOFtors for advanced practical scenarios, it is necessary to investigate the reticular protective mechanism, making it theoretically understandable, especially from the interaction between inorganic and biological interface.[28]

Nowadays, bladder cancer still remains a global health concern, characterized by a high recurrence rate due to distinct molecular subtypes and low penetration across the tumor mass.[10,29] Traditional chemotherapy-based intravesical instillation therapy is limited by inefficient drug delivery, multiple instillation sessions, and poor lesion retention, making bladder cancer treatment painful and costly.[30] In this study, we designed anti-biopassivated reticular motors with sustained locomotion lifetime against complex physiological environments for the first time and explored their potential application in bladder cancer therapy. The urease-powered MOF motors (Ur-MOFtors) were constructed by conjugating zeolitic imidazolate framework-90 (ZIF-90)[31,32] with urease under a mild synthetic condition. Based on preserving activity and the extended circulating lifespan of urease, this Ur-MOFtor exhibited continuous motion for at least 90 min, which was an 18-fold increase in locomotion lifetime compared with urease adsorbed onto the surface of MOFs. The prolonging movement duration of Ur@MOFtor was attributed to the ease of hydrogen bond formation between ammonia (NH_3, one of the products of the urease-catalyzed reaction) and the 2-imidazolate carboxaldehyde ligand, which was further elucidated by *in situ* Fourier transform infrared (FTIR) spectroscopy and theory calculations of hydrogen bond binding energy. Given its resistance to biological passivation and circulated lifespan, we successfully applied Ur-MOFtors to load doxorubicin (Dox) for the treatment of orthotopic bladder cancer. The persistent motion of Dox-loaded Ur-MOFtors (Dox@Ur-MOFtors) in urea promoted the targeted accumulation, prolonged retention, and controlled Dox release at bladder cancer cell sites, achieving a high tumor inhibition rate with few bladder instillation sessions. The anti-biopassivated reticular platforms offer valuable insights for designing the sustained self-propulsion motor at the highly concentrated substrates in broad biomedical applications.

RESULTS AND DISCUSSION

Fabrication and Characterization of Ur-MOFtor. As illustrated in Figure 1a, Ur@ZIF-90 was assembled by embedding urease into MOFs through an *in situ* encapsulation approach under mild reaction conditions (room temperature and water solvent), which was also defined as Ur-MOFtor. Ur@ZIF-90 displayed an X-ray powder diffraction (XRD) pattern identical to that of pure ZIF-90 (Figure 1b), indicating the preservation of the crystalline reticular structure, even in the presence of urease. After urease was introduced into ZIF-90 with a loading rate of 5.9 wt % (Figure S1), the resulting Ur@ZIF-90 demonstrated a uniform rhombic dodecahedron structure with an approximate size of 2 μm as characterized by scanning electron microscopy (SEM, Figure S2), atomic force microscopy (Figure S3) image, and average hydrodynamic diameter analysis (Figure S4a). Moreover, the main element peaks in X-ray photoelectron spectroscopy (XPS) matched perfectly in both ZIF-90 and Ur@ZIF-90, and no characteristic

https://doi.org/10.1021/jacs.5c02949
J. Am. Chem. Soc. 2025, 147, 17936−17945

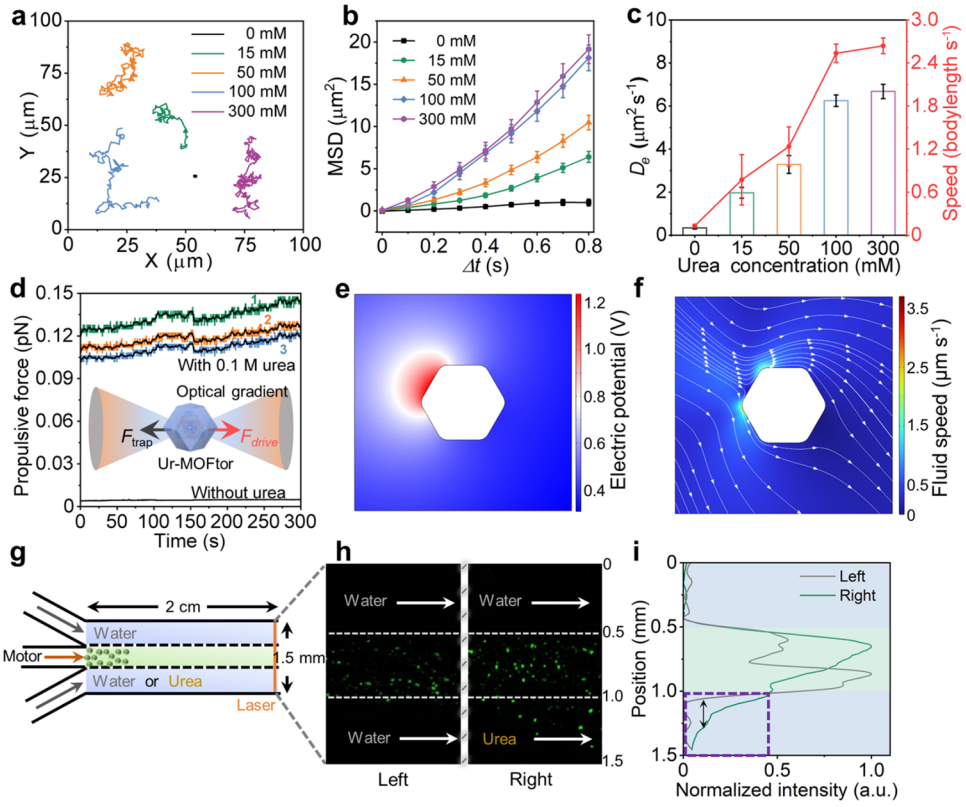

Figure 2. (a) Typical tracking trajectories of Ur-MOFtors within 15 s. (b) MSD plots, (c) D_e and average speed of Ur-MOFtors in different urea concentrations. Error bars indicate means ± SD (n = 10). (d) Curves of propulsive force dynamics of 3 independent Ur-MOFtors measured by optical tweezer with 0.1 M urea (colored lines) and without urea (gray line). Inset: A schematic illustration of the force balance between the optical trap and Ur-MOFtor. COMSOL simulation of (e) electrical potential distribution (color code) and (f) flow field (white arrow) around Ur-MOFtor in urea solution. (g) A schematic illustration of microfluidic chip structure. (h) Representative fluorescence microscopy image of microfluidic channels under continuous injection (from top to bottom) with water, FITC-labeled Ur-MOFtors, and water (left) or urea (right). Images acquired at the terminal end of the chip. (i) Corresponding normalized fluorescence intensity profile with different positions. The purple rectangle area denotes the difference in fluorescence intensity between water and urea channels at the bottom.

peaks (S and Ni) of urease were observed (Figure 1c), indicating that no urease may be adsorbed onto the surface of ZIF-90. Meanwhile, ζ-potential measurements showed that even after the introduction of negatively charged urease, the resulting Ur@ZIF-90 remains positively charged (Figure S4b), further suggesting that urease was likely encapsulated within MOFs. Next, confocal microscopy revealed the fluorescence distribution of urease within ZIF-90 (Figures 1d and S5), confirming that urease was confined inside MOF rather than adsorbed on its surface. As shown in Figure 1e, Fourier transform infrared (FTIR) spectra of urease and Ur@ZIF-90 had a prominent mode centered at 1670 cm^{-1}, extending from 1785 to 1575 cm^{-1}, that was attributed to a −C═O stretch.[33] Furthermore, we used second derivative spectra to reflect the precise structure of trapped urease in ZIF-90. As shown in Figure 1f, the amide I peaks associated with α-helix (1655 and 1641 cm^{-1}) and β-sheet (1633 cm^{-1}) modes of encapsulated urease remained nearly unchanged compared with free urease, indicating the perfectly preserved secondary structure of urease within ZIF-90.[34] Finally, the Zn^{2+} retention rate of Ur@ZIF-90 was calculated to be 98% after 15 min of incubation with a high concentration of urea (Figure S6), suggesting that the Ur@ZIF-90 structure was stable in urea due to its negligible decomposition.

Enzymatically Actuated Propulsion of Ur-MOFtors. The motion performance of Ur-MOFtors was systematically investigated through an inverted optical microscope under different fuel conditions. Typically, tracking trajectories of Ur-MOFtors displayed enhanced diffusion with the increase of urea concentrations (Figure 2a and Video S1). The extended diffusion radius in macroscopic trajectory also indicated the synchronized movement of the motor cluster in response to urea solutions (Figure S7). Mean square displacement (MSD) versus the time interval (Δt) with varied urea concentrations was obtained by extracted 2D coordinates (x, y) along the trajectories. The MSD values (Figure 2b) increased from 1.18 to 20.35 μm^2 with the growth of urea concentration in the range of 0−300 mM. And the curve shape transformed from a linear type (0 mM) to an exponential trend (15−300 mM), suggesting the motion pattern of Ur-MOFtors shifted from Brownian motion to proactively enhanced self-propulsion.[35] The effective diffusion coefficient (D_e) was calculated according to the equation D_e = 0.25 MSD/Δt. In Figure 2c (colored histograms), the D_e value of Ur-MOFtors was obtained to be 6.68 ± 0.33 μm^2 s^{-1} at 300 mM urea, which increased by about 18.7-fold compared with the D_e value of 0.34 ± 0.05 μm^2 s^{-1} without urea. The velocity of Ur-MOFtors (Figure 2c, red line) displayed 2.60 bodylength s^{-1} at 300 mM urea, exhibiting fast mobility of Ur-MOFtors in high urea concentrations. These results identified that the Ur-MOFtors possessed a urea-concentration-dependent enhanced diffusion.

https://doi.org/10.1021/jacs.5c02949
J. Am. Chem. Soc. 2025, 147, 17936−17945

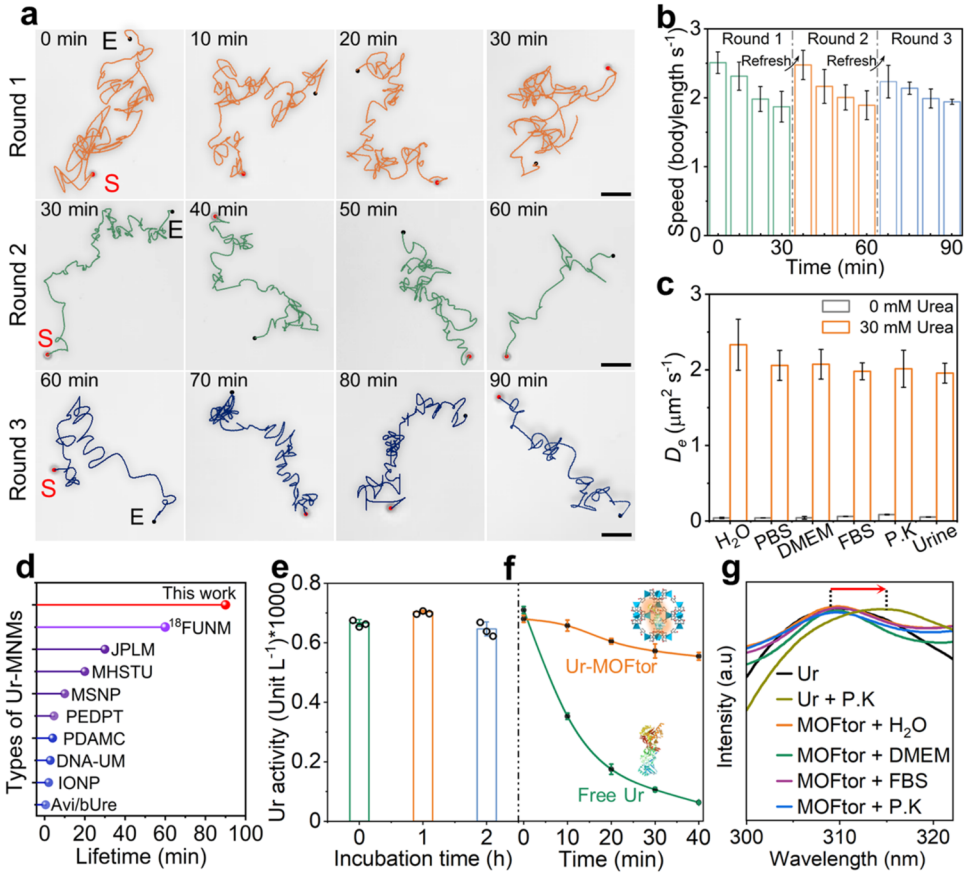

Figure 3. (a) Self-propulsion trajectories (scale bar: 10 μm) and corresponding (b) speeds of Ur-MOFtors during three consecutive repeated 30 min incubation rounds in 0.1 M urea. S: starting point; E: Ending point. (c) D_e in different media and simulated urine. DMEM: Dulbecco's modified Eagle's media; FBS: fetal bovine serum; P.K: Proteinase K. (d) Lifetime of Ur-MOFtors compared with other recently reported Ur-MNMs. (e) Urease activity of Ur-MOFtors in 0.1 M urea at different incubation times. (f) Continuous activity monitoring of Ur-MOFtor and free urease. (g) Fluorescence emission spectroscopy of urease in different conditions.

To explore the self-driving dynamics of single motors, we employed optical tweezers to quantify the propulsive force as a function of time. We observed that the propulsion force remained stable at 0.11 pN for 5 min (Figure 2d), suggesting the MOFtor's capacity for sustained movement. The random distribution of urease in ZIF-90 could lead to spatially asymmetrical enzyme catalysis[36] and thus generate the actuated propulsion for active movement of Ur-MOFtors in urea solutions. Moreover, we performed a COMSOL simulation under certain parameters to understand the propulsion mechanism of Ur-MOFtors (Table S1). In this numerical modeling, considering NH_4^+ and OH^- as the main products, an electric field is quickly established to maintain charge equilibrium outside the electric double layers (Figure 2e),[16,37] since the ion mobility of OH^- is much higher than that of NH_4^+. Against the electric field, an electro-osmotic flow forms around the negatively charged urease pointing toward the inner of the framework (Figure 2f), leading to the opposite movement of Ur-MOFtors. Near the motor, the consumed urea and the produced NH_3 exhibit opposite concentration gradients from the motor to the bulk solution (Figure S8), which reflects reasonable substance distribution in the catalytic process. Overall, these simulation results illustrate the directionality of Ur-MOFtors driven by ionic self-diffusiophoresis mechanism.[38]

The chemotactic behavior of Ur-MOFtors was evaluated using a three-inlet, one-outlet microfluidic chip under fluorescence microscopy. As seen in Figure 2g, water was injected into the upper channel and the bottom channel was filled with water or urea, respectively. When the flow rates remained constant, Ur-MOFtors were pumped into the middle channel for 2 min. Fluorescence images acquired under both dynamic (Figure 2h) and static (Figure S9) conditions showed that motor flow spontaneously moved toward the urea channel rather than the water channel. A clear preferential spreading of Ur-MOFtors was further quantified by monitoring the normalized fluorescent intensity in the 1.0−1.5 mm range (purple rectangle area) along the width of the microchannel (Figure 2i). The positive chemotaxis toward urea provides a directional accumulation of Ur-MOFtors on the tumor cell surface,[39] which promotes their effective functions in the urea-rich environment, especially in the bladder.

Sustained Locomotion Lifespan and Anti-biopassivation Mechanism. The motion sustainability of Ur-MOFtors was evaluated by repeatedly incubating them with 0.1 M urea and recording their mobility performance in repetitive rounds (Figure S10). The tracking trajectories recorded by both bright-field (Figure 3a and Video S2) and fluorescence microscopy (Video S3) showed a straight-line distance exceeding 60 μm within 15 s, suggesting powerful mobility even after prolonged exposure to high urea concentration for 90 min. The overlay image of time-lapse photography (Figure S11, 2 s per frame) clearly showed that Ur-MOFtors moved at a relatively uniform and regular speed

https://doi.org/10.1021/jacs.5c02949
J. Am. Chem. Soc. 2025, 147, 17936−17945

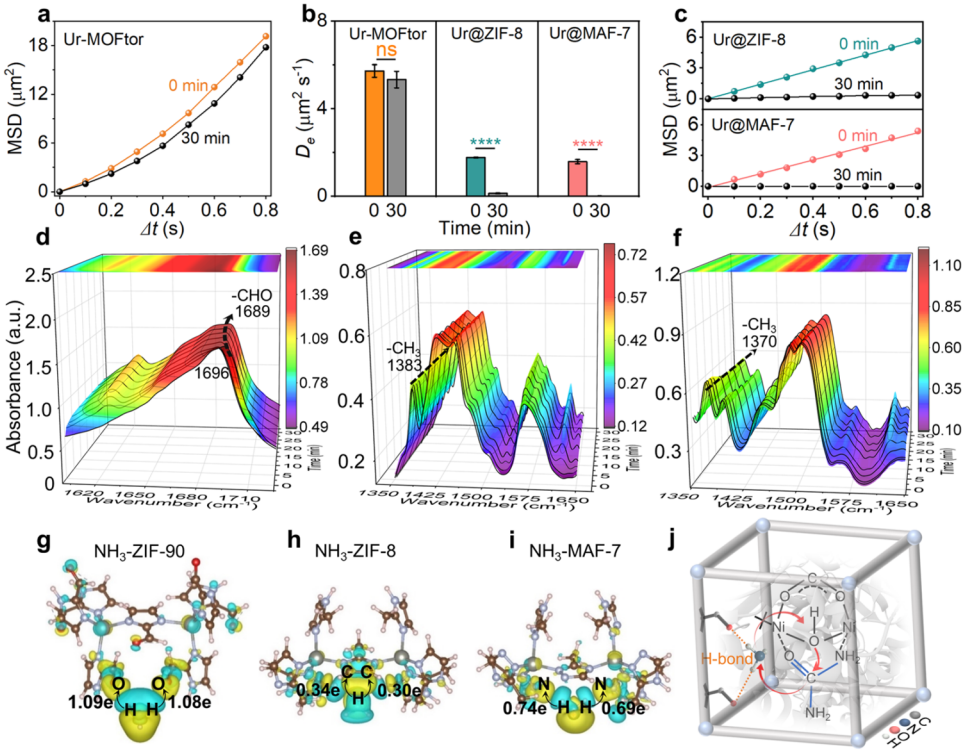

Figure 4. (a) MSD curves of Ur-MOFtor. (b) D_e of Ur-MOFtor, Ur@ZIF-8, and Ur@MAF-7 at 0 and 30 min. The asterisks (*) denote statistical differences: ****$p < 0.0001$, $p > 0.05$ represents not significant (ns). (c) MSD curves of Ur@ZIF-8 and Ur@MAF-7 at 0 and 30 min. *In situ* FTIR spectra of NH_3 adsorbed on (d) ZIF-90, (e) ZIF-8, and (f) MAF-7 at 0, 1, 3, 5, 10, 15, 20, 25, and 30 min, individually. Charge density difference and Bader charge of NH_3 adsorbing on (g) ZIF-90, (h) ZIF-8, and (i) MAF-7. The cyan and yellow areas represent electron depletion and accumulation, respectively. Color code for atoms: Zn, shift-gray; O, red; C, brown; N, light purple; H, light pink. (j) A schematic illustration of H-bond interaction promoted anti-biopassivation process of Ur-MOFtors.

in urea. During the 1st round (Figure 3b), the motor speed decreased slightly over time with a loss rate below 26%. When the motor was placed in a refreshed fuel environment, the maximum speed in the 2nd round (2.45 bodylength s^{-1}) and 3rd round (2.30 bodylength s^{-1}) remained close to that of the 1st round (2.50 bodylength s^{-1}), indicating that Ur-MOFtors possessed refreshable motion properties for at least 90 min, as well as in simulated urine containing 0.1 M urea (Figure S12). The sustained locomotion lifespan without significant speed decline was related to the stable crystal structure of Ur-MOFtors (Figure S13). D_e values of Ur-MOFtors remained almost unchanged in different media (Figure 3c), which was attributed to the protective effect of unique reticular structure.[40] These results confirmed that Ur-MOFtors could self-propel in various biological media (Video S4), even after 14 days of storage (Figure S14). Compared with Ur-MNMs based on other materials (Figure 3d),[9,11,16,17,41−45] the proposed Ur-MOFtors exhibited a longer or comparable motion lifespan, highlighting the significance of MOF in promoting enzyme resistance to biological passivation.

We then measured the urease activity of Ur-MOFtors to understand its role in preserving sustained mobility. As shown in Figure 3e, the urease activity of Ur-MOFtors was kept constant even when the incubation time with urea was extended to 120 min, suggesting the motor's lasting lifespan. Specifically, during continuous enzyme activity monitoring, the activity decay rate of free urease was 5.2 times higher than that of Ur-MOFtors (Figure 3f), demonstrating the anti-biopassivation of Ur-MOFtors in the catalytic process. Meanwhile, this was under 278 nm light excitation (Figure S15), the spectra of Ur-MOFtors in different biological media all displayed a peak at 309 nm, which was consistent with the spectral curve of free urease in water (Figure 3g). On the contrary, this peak red-shifted to 314 nm when placing free urease in proteinase K medium, denoting structural damage to urease. These phenomena explained the vulnerability of free urease in complex environments and emphasized the advantages of reticular structure in stabilizing enzyme structure. Moreover, Ur-MOFtors showed identical emission profiles within 24 h (Figure S16), proving the long-lasting stabilizing effect of MOFs on the urease structure.

Next, we explored the dynamic process of anti-biopassivation in the presence of 0.1 M urea. MSD and D_e of Ur-MOFtors exhibited no significant difference at 0 and 30 min (Figure 4a,4b, left), indicating sustained propulsion of Ur-MOFtors over time. For a comparison, two other types of Ur@MOF composites, namely, Ur@ZIF-8 and Ur@MAF-7 were synthesized and characterized with the SEM images (Figure S17) and XRD patterns (Figure S18). The urease loading of Ur@ZIF-8 and Ur@MAF-7 was determined to be 6.27 and 8.52 wt %, respectively (Figure S19a and Table S2). The motion durations of Ur@ZIF-8 and Ur@MAF-7 in the presence of 0.1 M urea were far less than 30 min (Figure 4c and Video S5), indicating the limited protective effect of ZIF-8 and MAF-7 on the urease activity. The comparison of activity tests showed that Ur-MOFtors had the greatest urease activity of 545 U L^{-1} comparable to free urease at a high concentration of urea (Figure S20), which was beneficial from the reticular structures. Besides, to verify the microenvironment effect of MOFs, we immobilized urease onto the surface of ZIF-90,

https://doi.org/10.1021/jacs.5c02949
J. Am. Chem. Soc. 2025, 147, 17936−17945

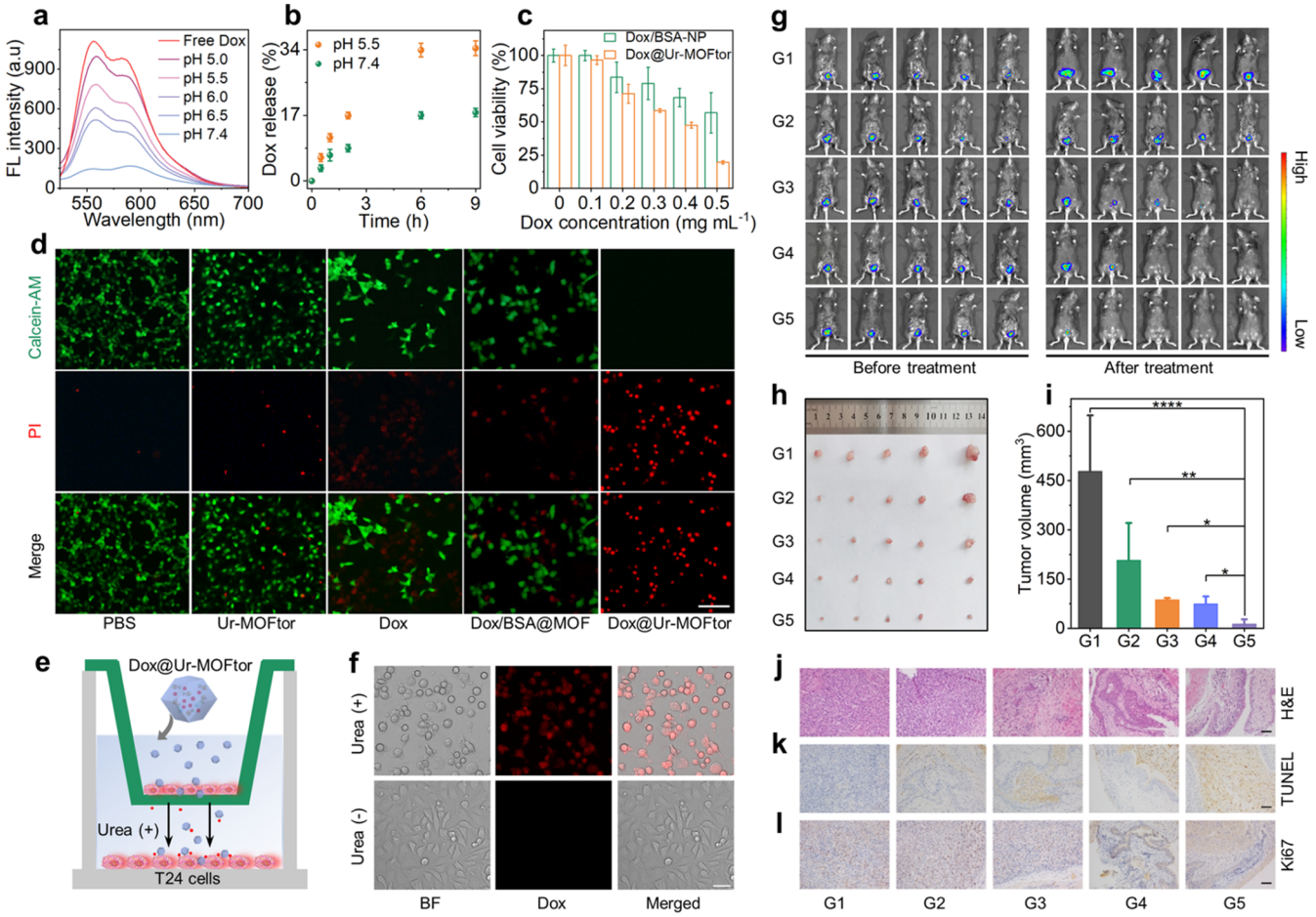

Figure 5. (a) Fluorescence emission spectra of Dox released by Dox@Ur-MOFtors at different pH levels. (b) Release profiles of Dox from Dox@Ur-MOFtors in pH 5.5 and 7.4 PBS containing 0.1 M urea. (c) Cell viability of T24 cells incubated with Dox/BSA-NPs and Dox@Ur-MOFtors in 0.1 M urea (pH 5.5). (d) Live/dead staining of T24 cells with 3 h of incubation in 0.1 M urea (pH 5.5) using Calcein-AM and PI (scale bar: 200 μm). (e) A schematic illustration and (f) fluorescence images for intercellular space penetration of Dox@Ur-MOFtors in the presence (Urea (+)) and absence (Urea (−)) of 0.1 M urea. Red channel (Dox) fluorescence was collected at 555−605 nm with 488 nm excitation (scale bar: 50 μm). (g) *In vivo* bioluminescence images of tumors in mice in each group before (left) and after (right) treatment. The bladder instillation regimen is divided into five groups: PBS (G1), Ur-MOFtor (G2), Dox (G3), Dox/BSA-NP (G4), and Dox@Ur-MOFtor (G5). (h) Morphology and (i) the corresponding volume of excised bladder and tumor tissues from each treatment group. The asterisks (*) denote statistical differences: ****p < 0.0001, **p < 0.01, *p < 0.05. (j) H&E staining, (k) TUNEL, and (l) Ki67 immunohistochemical staining images of the excised bladder and tumor tissue from each treatment group. Scale bars: 100 μm.

denoted as Ur-on ZIF-90 as confirmed by confocal imaging (Figure S21a). The resulting Ur-on ZIF-90 particle moved for only less than 5 min in 0.1 M urea (Figure S21b−d), indicating the important role of the intrareticular microenvironment of MOFs in protecting urease activity.

Furthermore, *in situ* FTIR spectra were conducted to characterize the interactions between NH_3 and MOFs. As shown in Figure 4d, the peak centered at 1696 cm^{-1} belonging to −C═O stretch vibration gradually red-shifted to 1689 cm^{-1} with the passage of adsorption time, attributing to decreased energy of carbonyl group from ZIF-90. This reflected the interaction between the carbonyl group on the side chain of the imidazole skeleton and NH_3. However, the bending vibration of $-CH_3$ in ZIF-8 (Figure 4e) and MAF-7 (Figure 4f) kept constant even after adsorbing NH_3, which implied the weak interaction in these two MOFs. In fact, Michaelis constants (K_m) of three types of urease-MOF composites (Figure S19b−d) were determined by measuring NH_3 production using the indophenol method.[46,47] Compared with Ur@ZIF-8 (2.3 mM) and Ur@MAF-7 (3.12 mM), Ur-MOFtors had the smallest K_m of 1.77 mM, demonstrating the strong affinity between the substrate and urease in ZIF-90.

Charge and energy analyses of the three types of MOFs before and after NH_3 adsorption were performed by DFT calculations. Optimized structure shows that each NH_3 molecule with adjacent ligands can form two hydrogen bonds (N−H···O), with H−O bond lengths of 2.278 and 2.331 Å (Figure S22). Charge density difference described electron accumulation around the carbonyl group, and Bader charge quantified O atoms of the carbonyl group gaining 1.09 and 1.08 electrons from two hydrogen atoms of NH_3, respectively (Figure 4g). These results suggest efficient charge transfer between NH_3 and ligands of ZIF-90. In comparison, the charge transfer process in ZIF-8 (Figure 4h) and MAF-7 (Figure 4i) is inefficient due to less electron flowing into imidazole skeletons, indicating that both ZIF-8 and MAF-7 have weaker adsorption capacity for NH_3 than ZIF-90. More intuitively, the adsorption energy of NH_3 on ZIF-90 was calculated as −0.47 eV, which is higher than −0.22 eV on ZIF-8 and −0.34 eV on MAF-7 (Figure S23). These findings

https://doi.org/10.1021/jacs.5c02949
J. Am. Chem. Soc. 2025, 147, 17936−17945

demonstrate that hydrogen bonds are easily formed in ZIF-90. Combined with the mechanism of urease-catalyzed urea hydrolysis[48,49] and the deactivation of urease attacked by NH_3,[14,15,50] we proposed the intrinsic molecular mechanism of ZIF-90 in stabilizing urease activity and achieving continuous movement of Ur-MOFtors. That is, in the presence of ZIF-90, the hydrogen bonds strengthen the interaction between NH_3 and the skeleton, enhancing NH_3 adsorption, suppressing its reactivity, and thereby preserving the enzyme's catalytic capacity (Figure 4j). Overall, the hydrogen bond-rich microenvironment in the framework promotes significantly both the longevity of self-propelled mobility and the stability of structural integrity, providing a potential for Ur-MOFtors in biomedical fields, particularly in bladder cancer treatment.

Ur-MOFtors as Drug Delivery Vehicles in Bladder Cancer Therapy. To endow the motor with chemotherapy properties, doxorubicin (Dox) was encapsulated inside Ur-MOFtors to achieve a high loading rate of 2.0 wt % (Figure S24). We assessed the drug release profiles of Dox@Ur-MOFtors as a motor-driven system in response to the acidic environment. As the pH decreased, the fluorescence intensity of Dox gradually increased (Figure 5a), which proved that Ur-MOFtors can effectively release Dox within the pH range of 5−6, as evidenced by pH dynamics of Ur-MOFtors in 0.1 M urea solution (Figure S25). In pH 5.5 PBS, the release rate of Dox reached a plateau after 9 h, at approximately 34% (Figures 5b and S26), indicating the potential to kill tumor cells due to continuous Dox diffusion. To test the enhanced drug delivery of Dox@Ur-MOFtor, we set up a control group, using bovine serum albumin (BSA) instead of urease to prepare Dox/BSA-nanoparticles (Dox/BSA-NPs). As shown in Figure 5c, at the concentration of 0.5 mg mL^{-1}, the cell viability of Dox@Ur-MOFtor group (19%) was much lower than that of Dox/BSA-NP group (57%) and free Dox group (46%) under 3 h incubation (Figure S27), which was related to the enhanced diffusion properties of Ur-MOFtors. Meanwhile, the killing effect of Dox@Ur-MOFtor on human bladder transitional T24 cells was visualized by Calcein-AM and propidium iodide (PI) staining (Figures 5d and S28). The PBS and MOFtor groups were almost completely covered by the green fluorescence of the Calcein-AM channel. The Dox and Dox/BSA-NPs groups were partially covered by green fluorescence. However, with the addition of Dox@Ur-MOFtor, the PI channel gradually showed red fluorescence, confirming the enhanced chemotherapy efficacy of Dox@Ur-MOFtor. Both the CCK-8 assay in the Ur-MOFtor group (Figure S29) and live/dead cell staining in the Ur-MOFtor group without urea (Figure S30) consistently demonstrated high cell viability, indicating that urease-driven propulsion introduces minimal enzymatic toxicity. Similarly, flow cytometry analysis showed a late apoptosis rate of 78.3% under Dox@Ur-MOFtor's treatment, which was much higher than that of other groups (Figure S31). These data revealed that the sustained mobility and enhanced accumulation of biocompatible Dox@Ur-MOFtor promoted the efficiency of drug-based therapy (Figure S32).

The capability of Dox@Ur-MOFtor to penetrate different cell layers in tissue was assessed with Transwell experiments. A two-dimensional cellular model was established by seeding T24 cells in both the upper and the lower chambers (Figure 5e). The T24 cells were treated with Dox@Ur-MOFtor in the presence and absence of urea, respectively. Dox fluorescence was negligible from T24 cells that seeded in the lower chamber for the group in the absence of urea (Figure 5f, urea (−)), while strong Dox fluorescence was observed from T24 cells for the group with urea (Figure 5f, urea (+)). These results indicated that the urea-fueled Ur-MOFtors could realize efficient penetration of intercellular space and drug release for active therapy within the urea-rich environment in the bladder (Figure S33).

In vivo experiments were conducted using a C57BL/6J mouse orthotopic bladder tumor model to evaluate the antitumor efficacy of MOFtors (Figure S34). The model was established by surgically inoculating luciferase-expressing MB49 cells onto the bladder wall of C57BL/6J mice, followed by suturing and a 2 week incubation period. Tumor-bearing mice were randomly divided into 5 groups (n = 5 per group) and treated with intravesical instillation of PBS (control), Ur-MOFtor, Dox, Dox/BSA-NP, or Dox@Ur-MOFtor. Intravesical administration started on day 2 and was repeated on days 4 and 6. Antitumor effects were assessed on day 9. Bioluminescence imaging of luciferase-labeled MB49 cells confirmed successful tumor establishment in all mice (Figure 5g, left). Throughout the experiment, the body weights of all groups remained stable (Figure S35). In the presence of 0.1 M urea in acidic PBS, active Dox@Ur-MOFtor (Figure 5g−i, Group 5) demonstrated the best antitumor effect, with significant tumor shrinkage or even complete disappearance, far outperforming the other treatment groups.

After treatment, H&E staining images of the bladder and tumor tissues showed fewer heterogeneous tumor cells in the Dox@Ur-MOFtor group (Figure 5j, Group 5) compared with the other treatment groups, indicating enhanced tumor treatment efficacy due to the synergistic effect of MOFtors and Dox. Additionally, TUNEL staining (Figure 5k, Group 5) was higher in the Dox@Ur-MOFtor group, suggesting increased apoptosis, while Ki67 staining (Figure 5l, Group 5) was reduced, indicating decreased tumor proliferative potential. These results demonstrate that Dox@Ur-MOFtor provides effective treatment for orthotopic bladder cancer in mice. Moreover, H&E staining of the major organs (heart, liver, spleen, lungs, and kidneys) collected from mice at the end of the treatment (Figure S36) showed no significant damage in any treatment group, indicating the satisfactory *in vivo* biosafety of both Ur-MOFtor and Dox@Ur-MOFtor. Thanks to the sustained locomotion lifetime and enhanced targeting penetration in the bladder, Ur-MOFtor-based chemotherapy offers distinct benefits including less instillation frequency (three times) and shorter treatment duration (five-day instillation cycle) compared with other related approaches.[51−53] Overall, anti-biopassivated Ur-MOFtors are endowed with the unique advantages of stable activity and sustained motion lifespan in a urea-rich environment, serving as a versatile delivery drug vehicle for improved antitumor efficacy against orthotopic bladder cancer.

CONCLUSIONS

In summary, we successfully established anti-biopassivated reticular micromotors based on hydrogen bond-rich MOFs for bladder cancer therapy. Ur-MOFtors embedding urease into the framework enabled a high enzymatic activity comparable to native urease even in high-concentration urea conditions. The propulsion pathway of Ur-MOFtor was driven through ionic diffusiophoresis with positive chemotaxis toward urea. Importantly, such an MOFtor exhibited excellent anti-biopassivation and sustained motion lifespan for at least 90 min in urea-rich conditions. The remarkable features were

https://doi.org/10.1021/jacs.5c02949
J. Am. Chem. Soc. 2025, 147, 17936−17945

identified by the hydrogen bonds protection effect against catalytically produced NH_3, highlighting the significance of the intrareticular hydrogen bond-rich microenvironment of MOF in optimizing the functionality of Ur-MOFtor. By taking advantage of the intrinsic property of enhanced penetration, Ur-MOFtor was utilized for effective orthotopic bladder cancer therapy with few instillation sessions and short treatment cycles. In a word, this study presents a novel paradigm of anti-biopassivated urease-powered reticular motors with long-lasting motion lifespan, providing a reliable approach to bladder cancer therapy.

■ ASSOCIATED CONTENT

Supporting Information

The Supporting Information is available free of charge at https://pubs.acs.org/doi/10.1021/jacs.5c02949.

Representative motion trajectories of Ur-MOFtors in different concentrations of urea (Video S1) (MP4)

The continuous motion of Ur-MOFtors in 100 mM urea during 30 min (Video S2) (MP4)

Continuous tracking trajectories recorded at 0, 30, 60, and 90 min by fluorescence microscopy (Video S3) (MP4)

Representative motion trajectories of Ur-MOFtors under different media containing 100 mM urea (Video S4) (MP4)

The motion trajectories of Ur@ZIF-8 (top) and Ur@MAF-7 (bottom) in 100 mM urea at 0 and 10 min (Video S5) (MP4)

Materials and methods, detailed synthesis, motion analysis, and DFT calculations on anti-biopassivated Ur-MOFtors (PDF)

■ AUTHOR INFORMATION

Corresponding Authors

Jie Wu − *State Key Laboratory of Analytical Chemistry for Life Science, School of Chemistry and Chemical Engineering, Nanjing University, Nanjing 210023, China;* orcid.org/0000-0003-1379-122X; Email: wujie@nju.edu.cn

Jianping Lei − *State Key Laboratory of Analytical Chemistry for Life Science, School of Chemistry and Chemical Engineering, Nanjing University, Nanjing 210023, China;* orcid.org/0000-0002-3594-180X; Email: jpl@nju.edu.cn

Authors

Jun Sun − *State Key Laboratory of Analytical Chemistry for Life Science, School of Chemistry and Chemical Engineering, Nanjing University, Nanjing 210023, China*

Ran Chu − *Department of Obstetrics and Gynecology, Shandong Provincial Hospital Affiliated to Shandong First Medical University, Shandong First Medical University, Jinan 250021, China*

Xiaoqian Wu − *State Key Laboratory of Analytical Chemistry for Life Science, School of Chemistry and Chemical Engineering, Nanjing University, Nanjing 210023, China*

Qian Yu − *State Key Laboratory of Analytical Chemistry for Life Science, School of Chemistry and Chemical Engineering, Nanjing University, Nanjing 210023, China*

Wencheng Xiao − *State Key Laboratory of Analytical Chemistry for Life Science, School of Chemistry and Chemical Engineering, Nanjing University, Nanjing 210023, China*

Hang Ao − *State Key Laboratory of Analytical Chemistry for Life Science, School of Chemistry and Chemical Engineering, Nanjing University, Nanjing 210023, China*

Yuru Wang − *State Key Laboratory of Analytical Chemistry for Life Science, School of Chemistry and Chemical Engineering, Nanjing University, Nanjing 210023, China*

Taikang Wu − *State Key Laboratory of Analytical Chemistry for Life Science, School of Chemistry and Chemical Engineering, Nanjing University, Nanjing 210023, China*

Huangxian Ju − *State Key Laboratory of Analytical Chemistry for Life Science, School of Chemistry and Chemical Engineering, Nanjing University, Nanjing 210023, China;* orcid.org/0000-0002-6741-5302

Complete contact information is available at: https://pubs.acs.org/10.1021/jacs.5c02949

Author Contributions

[§]J.S. and R.C. contributed equally to this work. The manuscript was written through the contributions of all authors. All authors have given approval to the final version of the manuscript.

Notes

The authors declare no competing financial interest.

■ ACKNOWLEDGMENTS

We gratefully acknowledge the National Natural Science Foundation of China (22274071 and 22234005) and the Jiangsu Basic Research Center for Synthetic Biology (BK20233003).

■ REFERENCES

(1) Sánchez, S.; Soler, L.; Katuri, J. Chemically Powered Micro- and Nanomotors. *Angew. Chem., Int. Ed.* **2015**, *54*, 1414−1444.

(2) Yao, D. R.; Kim, I.; Yin, S.; Gao, W. Multimodal Soft Robotic Actuation and Locomotion. *Adv. Mater.* **2024**, *36*, No. 2308829.

(3) Ma, X.; Hortelão, A. C.; Patiño, T.; Sánchez, S. Enzyme Catalysis To Power Micro/Nanomachines. *ACS Nano* **2016**, *10*, 9111−9122.

(4) Arqué, X.; Patiño, T.; Sánchez, S. Enzyme-Powered Micro- and Nano-Motors: Key Parameters for an Application-Oriented Design. *Chem. Sci.* **2022**, *13*, 9128−9146.

(5) Yuan, H.; Liu, X.; Wang, L.; Ma, X. Fundamentals and Applications of Enzyme Powered Micro/Nano-Motors. *Bioact. Mater.* **2021**, *6*, 1727−1749.

(6) Soto, F.; Karshalev, E.; Zhang, F.; de Avila, B. E. F.; Nourhani, A.; Wang, J. Smart Materials for Microrobots. *Chem. Rev.* **2022**, *122*, 5365−5403.

(7) Mujtaba, J.; Liu, J.; Dey, K. K.; Li, T.; Chakraborty, P.; Xu, K.; Makarov, D.; Barmin, R. A.; Gorin, D. A.; Tolstoy, V. P.; Huang, G.; Solovev, A. A.; Mei, Y. Micro-Bio-Chemo-Mechanical-Systems: Micromotors, Microfluidics, and Nanozymes for Biomedical Applications. *Adv. Mater.* **2021**, *33*, No. 2007465.

(8) Xu, D.; Hu, J.; Pan, X.; Sánchez, S.; Yan, X.; Ma, X. Enzyme-Powered Liquid Metal Nanobots Endowed with Multiple Biomedical Functions. *ACS Nano* **2021**, *15*, 11543−11554.

(9) Hortelão, A. C.; Patiño, T.; Perez-Jiménez, A.; Blanco, À.; Sánchez, S. Enzyme-Powered Nanobots Enhance Anticancer Drug Delivery. *Adv. Funct. Mater.* **2018**, *28*, No. 1705086.

(10) Tang, S.; Zhang, F.; Gong, H.; Wei, F.; Zhuang, J.; Karshalev, E.; de Avila, B. E. F.; Huang, C.; Zhou, Z.; Li, Z.; Yin, L.; Dong, H.; Fang, R.; Zhang, X.; Zhang, L.; Wang, J. Enzyme-Powered Janus Platelet Cell Robots for Active and Targeted Drug Delivery. *Sci. Robot.* **2020**, *5*, No. eaba6137.

(11) Simó, C.; Serra-Casablancas, M.; Hortelao, A. C.; Carlo, V. D.; Guallar-Garrido, S.; Plaza-García, S.; Rabanal, R. M.; Ramos-Cabrer, P.; Yagüe, B.; Aguado, L.; Bardia, L.; Tosi, S.; Gómez-Vallejo, V.;

Martín, A.; Patiño, T.; Julián, E.; Colombelli, J.; Llop, J.; Sánchez, S. Urease-Powered Nanobots for Radionuclide Bladder Cancer Therapy. *Nat. Nanotechnol.* **2024**, *19*, 554−564.
(12) Ye, Z.; Che, Y.; Dai, D.; Jin, D.; Yang, Y.; Yan, X.; Ma, X. Supramolecular Modular Assembly of Imaging-Trackable Enzymatic Nanomotors. *Angew. Chem., Int. Ed.* **2024**, *63* (16), No. e202401209.
(13) Valles, M.; Pujals, S.; Albertazzi, L.; Sánchez, S. Enzyme Purification Improves the Enzyme Loading, Self-Propulsion, and Endurance Performance of Micromotors. *ACS Nano* **2022**, *16*, 5615−5626.
(14) Vasudevan, P. T.; Ruggiano, L.; Weiland, R. H. Studies on the Deactivation of Immobilized Urease. *Biotechnol. Bioeng.* **1990**, *35*, 1145−1149.
(15) Vasdudevan, P. T.; Gokarn, Y. Deactivation of Jack Bean Urease in Urea Hydrolysis. *Appl. Biochem. Biotechnol.* **1996**, *60*, 49−61.
(16) Patino, T.; Porchetta, A.; Jannasch, A.; Lladó, A.; Stumpp, T.; Schäffer, E.; Ricci, F.; Sánchez, S. Self-Sensing Enzyme-Powered Micromotors Equipped with pH-Responsive DNA Nanoswitches. *Nano Lett.* **2019**, *19*, 3440−3447.
(17) Xu, D.; Zhou, C.; Zhan, C.; Wang, Y.; You, Y.; Pan, X.; Jiao, J.; Zhang, R.; Dong, Z.; Wang, W.; Ma, X. Enzymatic Micromotors as a Mobile Photosensitizer Platform for Highly Efficient On-Chip Targeted Antibacteria Photodynamic Therapy. *Adv. Funct. Mater.* **2019**, *29*, No. 1807727.
(18) Liu, T.; Xie, L.; Price, C. H.; Liu, J.; He, Q.; Kong, B. Controlled Propulsion of Micro/Nanomotors: Operational Mechanisms, Motion Manipulation and Potential Biomedical Applications. *Chem. Soc. Rev.* **2022**, *51*, 10083−10119.
(19) Arqué, X.; Romero-Rivera, A.; Feixas, F.; Patiño, T.; Osuna, S.; Sánchez, S. Intrinsic Enzymatic Properties Modulate the Self-Propulsion of Micromotors. *Nat. Commun.* **2019**, *10*, No. 2826.
(20) Furukawa, H.; Cordova, K. E.; O'Keeffe, M.; Yaghi, O. M. The Chemistry and Applications of Metal-Organic Frameworks. *Science* **2013**, *341*, No. 1230444.
(21) Yaghi, O. M.; Kalmutzki, M. J.; Diercks, C. S. *Introduction to Reticular Chemistry: Metal-Organic Frameworks and Covalent Organic Frameworks*; Wiley-VCH: Weinheim, Germany, 2019.
(22) Terzopoulou, A.; Nicholas, J. D.; Chen, X.; Nelson, B.; Pané, S.; Puigmartí-Luis, J. Metal-Organic Frameworks in Motion. *Chem. Rev.* **2020**, *120*, 11175−11193.
(23) Kim, J.; Mayorga-Burrezo, P.; Song, S.; Mayorga-Martinez, C. C.; Medina-Sánchez, M.; Pané, S.; Pumera, M. Advanced Materials for Micro/Nanorobotics. *Chem. Soc. Rev.* **2024**, *53*, 9190−9253.
(24) You, Y.; Xu, D.; Pan, X.; Ma, X. Self-Propelled Enzymatic Nanomotors for Enhancing Synergetic Photodynamic and Starvation Therapy by Self-Accelerated Cascade Reactions. *Appl. Mater. Today* **2019**, *16*, 508−517.
(25) Liu, J.; Huang, J.; Zhang, L.; Lei, J. Multifunctional Metal-Organic Framework Heterostructures for Enhanced Cancer Therapy. *Chem. Soc. Rev.* **2021**, *50*, 1188.
(26) Yang, Y.; Arqué, X.; Patiño, T.; Guillerm, V.; Blersch, P. R.; Pérez-Carvajal, J.; Imaz, I.; Maspoch, D.; Sánchez, S. Enzyme-Powered Porous Micromotors Built from a Hierarchical Micro- and Mesoporous UiO-Type Metal-Organic Framework. *J. Am. Chem. Soc.* **2020**, *142*, 20962−20967.
(27) Liu, X.; Wang, Y.; Wang, L.; Chen, W.; Ma, X. Enzymatic Nanomotors Surviving Harsh Conditions Enabled by Metal Organic Frameworks Encapsulation. *Small* **2024**, *20*, No. 2305800.
(28) Liu, Y.; Ge, J. Into the Unknown: Micro/Nanomotors Propelled by Biocatalysis Based on Metal-Organic Frameworks. *Chem. Catal.* **2022**, *2*, 2458−2470.
(29) Dyrskjøt, L.; Hansel, D. E.; Efstathiou, J. A.; Knowles, M. A.; Galsky, M. D.; Teoh, J.; Theodorescu, D. Bladder Cancer. *Nat. Rev. Dis. Primers* **2023**, *9*, 58.
(30) Bellat, V.; Michel, A. O.; Thomas, C.; Stokol, T.; Choi, B. B.; Law, B. A Urinary Drug-Disposing Approach as an Alternative to Intravesical Chemotherapy for Treating Nonmuscle Invasive Bladder Cancer. *Cancer Res.* **2022**, *82*, 1409−1422.
(31) Zhang, J.; Zhu, A.; Lin, R.; Qi, X.; Chen, X. Pore Surface Tailored SOD-Type Metal-Organic Zeolites. *Adv. Mater.* **2011**, *23*, 1268−1271.
(32) Morris, W.; Doonan, C. J.; Furukawa, H.; Banerjee, R.; Yaghi, O. M. Crystals as Molecules: Postsynthesis Covalent Functionalization of Zeolitic Imidazolate Frameworks. *J. Am. Chem. Soc.* **2008**, *130*, 12626−12627.
(33) Liang, W.; Xu, H.; Carraro, F.; Maddigan, N. K.; Li, Q.; Bell, S. G.; Huang, D.; Taraiz, A.; Solomon, M. B.; Amenitsch, H.; Vaccari, L.; Sumby, C. J.; Falcaro, P.; Doonan, C. J. Enhanced Activity of Enzymes Encapsulated in Hydrophilic Metal-Organic Frameworks. *J. Am. Chem. Soc.* **2019**, *141*, 2348−2355.
(34) Shivu, B.; Seshadri, S.; Li, J.; Oberg, K. A.; Uversky, V. N.; Fink, A. L. Distinct β-Sheet Structure in Protein Aggregates Determined by ATR-FTIR Spectroscopy. *Biochemistry* **2013**, *52*, 5176−5183.
(35) Patiño, T.; Arqué, X.; Mestre, R.; Palacios, L.; Sánchez, S. Fundamental Aspects of Enzyme-Powered Micro- and Nanoswimmers. *Acc. Chem. Res.* **2018**, *51*, 2662−2671.
(36) Patiño, T.; Feiner-Gracia, N.; Arqué, X.; Miguel-López, A.; Jannasch, A.; Stumpp, T.; Schäffer, E.; Albertazzi, L.; Sánchez, S. Influence of Enzyme Quantity and Distribution on the Self-Propulsion of Non-Janus Urease-Powered Micromotors. *J. Am. Chem. Soc.* **2018**, *140*, 7896−7903.
(37) Wang, W. Open Questions of Chemically Powered Nano- and Micromotors. *J. Am. Chem. Soc.* **2023**, *145*, 27185−27197.
(38) Feng, Y.; Yuan, Y.; Wan, J.; Yang, C.; Hao, X.; Gao, Z.; Luo, M.; Guan, J. Self-Adaptive Enzyme-Powered Micromotors with Switchable Propulsion Mechanism and Motion Directionality. *Appl. Phys. Rev.* **2021**, *8*, No. 011406.
(39) Chen, H.; Li, T.; Liu, Z.; Tang, S.; Tong, J.; Tao, Y.; Zhao, Z.; Li, N.; Mao, C.; Shen, J.; Wan, M. A Nitric-Oxide Driven Chemotactic Nanomotor for Enhanced Immunotherapy of Glioblastoma. *Nat. Commun.* **2023**, *14*, No. 941.
(40) Huang, S.; Kou, X.; Shen, J.; Chen, G.; Ouyang, G. "Armor-Plating" Enzymes with Metal-Organic Frameworks (MOFs). *Angew. Chem., Int. Ed.* **2020**, *59*, 8786−8798.
(41) Sugai, N.; Morita, Y.; Komatsu, T. Nonbubble-Propelled Biodegradable Microtube Motors Consisting Only of Protein. *Chem. - Asian J.* **2019**, *14*, 2953−2957.
(42) Fraire, J. C.; Guix, M.; Hortelao, A. C.; Ruiz-González, N.; Bakenecker, A. C.; Ramezani, P.; Hinnekens, C.; Sauvage, F.; Smedt, S. C. D.; Braeckmans, K.; Sánchez, S. Light-Triggered Mechanical Disruption of Extracellular Barriers by Swarms of Enzyme Powered Nanomotors for Enhanced Delivery. *ACS Nano* **2023**, *17*, 7180−7193.
(43) Choi, H.; Jeong, S. H.; Kim, T. Y.; Yi, J.; Hahn, S. K. Bioinspired Urease-Powered Micromotor as an Active Oral Drug Delivery Carrier in Stomach. *Bioact. Mater.* **2022**, *9*, 54−62.
(44) Himori, S.; Sakata, T. Wireless Electrochemical Detection of Enzyme-Driven Conductive Hydrogel Motor for Autonomous Mobile Biosensor. *Sens. Actuators, B* **2023**, *393*, No. 134239.
(45) Hortelao, A. C.; Simó, C.; Guix, M.; Guallar-Garrido, S.; Julián, E.; Vilela, D.; Rejc, L.; Ramos-Cabrer, P.; Cossío, U.; Gómez-Vallejo, V.; Patiño, T.; Llop, J.; Sánchez, S. Swarming Behavior and in Vivo Monitoring of Enzymatic Nanomotors within the Bladder. *Sci. Robot.* **2021**, *6*, No. eabd2823.
(46) Amtul, Z.; Follmer, C.; Mahboob, S.; Rahman, A. U.; Mazhar, M.; Khan, K. M.; Siddiqui, R. A.; Muhammad, S.; Kazmi, S. A.; Choudhary, M. I. Germa-γ-Lactones as Novel Inhibitors of Bacterial Urease Activity. *Biochem. Biophys. Res. Commun.* **2007**, *356*, 457−463.
(47) Weatherburn, M. W. Phenol-Hypochlorite Reaction for Determination of Ammonia. *Anal. Chem.* **1967**, *39*, 971−974.
(48) Jabri, E.; Carr, M. B.; Hausinger, R. P.; Karplus, P. A. The Crystal Structure of Urease from Kiebsiella Aerogenes. *Science* **1995**, *268*, 998−1004.
(49) Kistiakowsky, G. B.; Rosenberg, A. J. The Kinetics of Urea Hydrolysis by Urease. *J. Am. Chem. Soc.* **1952**, *74*, 5020−5025.

https://doi.org/10.1021/jacs.5c02949
J. Am. Chem. Soc. 2025, 147, 17936−17945

(50) Rajagopalan, K.; Handler, P.; Fridovich, I. Competitive Inhibition of Enzyme Activity by Urea. *J. Biol. Chem.* **1961**, *236*, 1059−1065.
(51) Wang, Y.; Chen, W.; Wang, Z.; Zhu, Y.; Zhao, H.; Wu, K.; Wu, J.; Zhang, W.; Zhang, Q.; Guo, H.; Ju, H.; Liu, Y. NIR-II Light Powered Asymmetric Hydrogel Nanomotors for Enhanced Immunochemotherapy. *Angew. Chem., Int. Ed.* **2023**, *62*, No. e202212866.
(52) Chen, W.; Wang, Y.; Hu, H.; Zhu, Y.; Zhao, H.; Wu, J.; Ju, H.; Zhang, Q.; Guo, H.; Liu, Y. NIR-II Light Powered Hydrogel Nanomotor for Intravesical Instillation with Enhanced Bladder Cancer Therapy. *Nanoscale* **2024**, *16*, 10273.
(53) Tang, S.; Tang, D.; Zhou, H.; Li, Y.; Zhou, D.; Peng, X.; Ren, C.; Su, Y.; Zhang, S.; Zheng, H.; Wan, F.; Yoo, J.; Han, H.; Ma, X.; Gao, W.; Wu, S. Bacterial Outer Membrane Vesicle Nanorobot. *Proc. Natl. Acad. Sci. U.S.A.* **2024**, *121*, No. e2403460121.

https://doi.org/10.1021/jacs.5c02949
J. Am. Chem. Soc. 2025, 147, 17936−17945